


Spin-wave mode reversal and anisotropy in bicomponent magnonic crystals

Chandan Kumar[✉], Pratap Kumar Pal[✉], and Anjan Barman^{✉*}

*Department of Condensed Matter and Materials Physics, S.N. Bose National Centre for Basic Sciences,
Block JD, Sector III, Salt Lake, Kolkata 700106, India*

 (Received 25 July 2023; revised 9 November 2023; accepted 19 January 2024; published 8 February 2024)

Bicomponent magnonic crystals (BMCs) are engineered metamaterials comprised of magnetic materials with contrasting properties that offer a wide range of tunability in spin-wave (SW) dynamics, making them highly relevant for modern magnonic and spintronic devices. Herein, the magnetic configuration driven SW dynamics of BMC, having Permalloy ($\text{Ni}_{80}\text{Fe}_{20}$) inclusion of circular and square shapes in $\text{Co}_{50}\text{Fe}_{50}$ matrix, have been extensively studied using ferromagnetic resonance spectroscopy and micromagnetic simulation. The experimentally obtained magnetic field dispersion confirms the theoretically predicted SW mode reversal. In this phenomenon, the SW mode with the highest frequency, typically excited in the region of high saturation magnetization under a higher applied bias field, undergoes a transition, becoming the mode with the lowest frequency as the applied field decreases. Furthermore, we observed mode splitting and mode merging alongside the conventional monotonic variation of SW modes with changes in the applied bias field. The numerically simulated mode profile shows the bias field dependent preferential spatial excitation of SW modes, originating from the spatial distribution of the demagnetizing field. The magnetic microstate dependent spatial distribution of the demagnetizing field leads to the creation, distortion, and annihilation of positively and negatively demagnetized channels, which act as roadways for SW propagation.

DOI: [10.1103/PhysRevB.109.075407](https://doi.org/10.1103/PhysRevB.109.075407)

I. INTRODUCTION

The quest for sustainable and environment-friendly technology has led to the emergence of the field of magnonics. Magnonics, the research field which employs spin waves (SWs) or their quanta, magnons, to generate, transmit, and process information in a periodically modulated magnetic media, called magnonic crystal (MC). MCs are metamaterials like photonic and phononic crystals but offer several advantages over them, owing to their lower energy consumption, smaller size, easier integrability, and compatibility with complementary metal-oxide semiconductor structures [1,2]. MCs with varying shape [3–6], lattice symmetry [7–9], lattice constant [10,11], composition, size [12], and configuration [13–16] provide the flexibility to tune various aspects of SW characteristics such as magnonic band structure, quantum coupling [16–18], propagation speed [19,20], mode characteristics, and others. The recent advancements in MCs have paved the way for a wide range of practical applications in SW-based communication devices, e.g., SW filters [21–23], magnonic waveguides [24–26], phase shifters [27], SW emitters [28–30], SW-based logic devices [31,32], transistors [33,34], as well as for cellular nonlinear networking [35]. The ability of magnonics to replace the current charge-based circuits creates an urgent need to explore the properties of SW dynamics in various MCs, including multicomponent MCs with interelement exchange and dipolar couplings.

The bicomponent MC (BMC), as the name suggests, consists of two different materials in which one material is embedded in the matrix of another, with contrasting magnetic

properties. BMCs possess prime advantages over unicomponent MCs such as dots, antidots, nanowires, nanorings and others, owing to interfacial exchange and dipolar coupling between two materials [36–39]. The initial theoretical and experimental studies in BMCs have provided evidence of the superior tunability of magnonic band structure and SW dynamics in one-dimensional (1D) [40] as well as two-dimensional (2D) [41–46] BMCs. In 2D arrays of alternate Co and Permalloy ($\text{Ni}_{80}\text{Fe}_{20}$; Py hereafter) nanodots, it has been shown that the Co nanodots act as amplifiers of dipolar coupling between the Py nanodots [45]. It has been observed in systems of Py inclusion in $\text{Co}_{50}\text{Fe}_{50}$ (CoFe) matrix that BMC drastically enhances the propagation speed of SWs [37,38], which can further be tuned by a subtle change of the filling fraction of constituent materials [36]. The demagnetizing field (H_{de}) plays a crucial role in tailoring SW properties in BMCs, as it either enhances or suppresses the effective field in constituent materials depending upon their magnetic properties [39,47]. The H_{de} -induced two channels of SW propagation have been obtained in BMC consisting of Co nanodisks embedded in a matrix of Py: one channel through the Co nanodisks and the other in the space between the nanodisks [39]. Recent theoretical studies convey that the influence of H_{de} in lower applied bias field (H_{app}) is responsible for tuning the magnonic band gap [48,49] as well as the reversal of modes [50], i.e., the highest frequency mode which generally gets excited in a high saturation magnetization region becomes the lowest frequency mode as H_{app} lowers. This notable study emphasizes the importance of the demagnetizing field in effectively reducing the applied bias fields to tune the magnonic band gap and facilitate the intriguing mode reversal phenomenon. However, there is a lack of experimental validation and exploration regarding the influence

*Corresponding author: abarman@bose.res.in

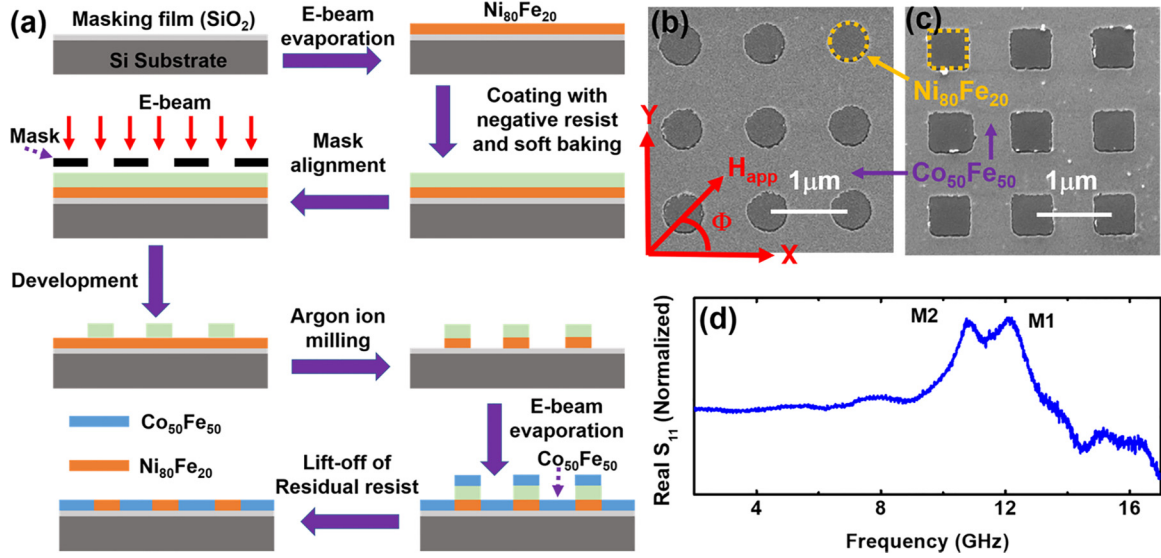


FIG. 1. (a) Schematic of the sample preparation method. The scanning electron microscopy image of (b) circular- and (c) square-shaped BMC. (d) Representative SW absorption spectra of circular-shaped BMC at an applied bias magnetic field, $H_{\text{app}} = 1.2$ kOe.

of configurational anisotropy on these phenomena. To address this research gap, our study focuses on BMCs and aims to extensively investigate the reversal of SW modes experimentally while emphasizing the role of magnetic microstates in shaping the dynamic characteristics of SWs. This research endeavor is driven by the dual objectives of advancing fundamental understanding in this field and exploring the potential applications that may arise from these phenomena.

Here, we employed ferromagnetic resonance spectroscopy and micromagnetic simulation to investigate the magnetic configuration driven magnetization dynamics in BMC with Py inclusion of circular and square shape in CoFe matrix. The configuration was fine-tuned by adjusting the in-plane orientation (Φ) of the H_{app} . In the experimentally obtained magnetic field dispersion at different Φ values, we have observed the mode reversal phenomenon, along with mode merging and splitting, associated with the monotonic variation of SW modes with H_{app} . The mode profiles have been studied using micromagnetic simulation to understand the origin and nature of the individual SW modes. The spatial maps of H_{de} at different Φ and its influence at different H_{app} have been investigated using micromagnetic simulation. The anisotropic nature of SW propagation at different configurations has also been numerically studied by exciting the SWs at the center of a simulated waveguide composed of BMC, to explore their potential applications in the field of magnonic waveguide engineering. Overall, our study provides a comprehensive analysis of the magnetic configuration driven magnetization dynamics in the BMC system, shedding light on the underlying mechanisms and offering valuable insights for potential technological advancements.

II. EXPERIMENTAL AND SIMULATION DETAILS

A. Sample fabrication

The 2D array of Py nanostructures embedded in a CoFe matrix [shown in Figs. 1(b) and 1(c)] was fabricated using

a combination of electron beam evaporation (EBE), electron beam lithography (EBL), and ion milling techniques. The diameter of the circular Py nanostructure is 500 nm ($\pm 5\%$), while in the square BMC, the side length of the Py nanostructure is 500 nm ($\pm 5\%$). The edge-to-edge separation between individual Py nanostructures is 550 nm ($\pm 5\%$) for both square and circular BMCs. The schematic of the sample preparation is depicted in Fig. 1(a). Using EBE, a 20-nm layer of Py was deposited over the self-oxidized Si[100] substrate in an ultra-high vacuum chamber with a base pressure of 2×10^{-8} Torr. The Py film was then coated with a single layer of negative resist (ma-N 2405) for EBL with a beam current of 100 pA to create the required pattern on top, followed by Ar ion milling at a base pressure of 1.8×10^{-4} Torr, which etched out all the Py film except the region under the exposed resist pattern. Subsequently, a 20-nm CoFe layer was deposited using EBE at a base pressure of 2×10^{-8} Torr, followed by a lift-off process. A 150-nm-thick coplanar waveguide (CPW) made of Au, with a width of 30 μm , a length of 300 μm , and a nominal characteristic impedance of 50 Ω , was patterned using maskless photolithography.

B. Measurement technique

The SW dynamics were measured in the frequency domain using broadband ferromagnetic resonance (FMR) spectroscopy techniques employing a vector network analyzer (VNA; PNA-L, Agilent, 10 MHz to 50 GHz) and a home-built probe station equipped with an in-built electromagnet that can rotate 360° within the sample plane. Microwave signals of varying frequencies were launched into the CPW through a ground-signal-ground (G-S-G) probe via a low-noise coaxial cable. The CPW was shorted at one end to measure the S_{11} scattering parameter in the reflection geometry after collecting data from the same G-S-G probe. The microwave frequency absorbed by the sample constituted the characteristic spectrum, recorded as the real and imaginary parts of the S_{11} parameter. To eliminate background noise,

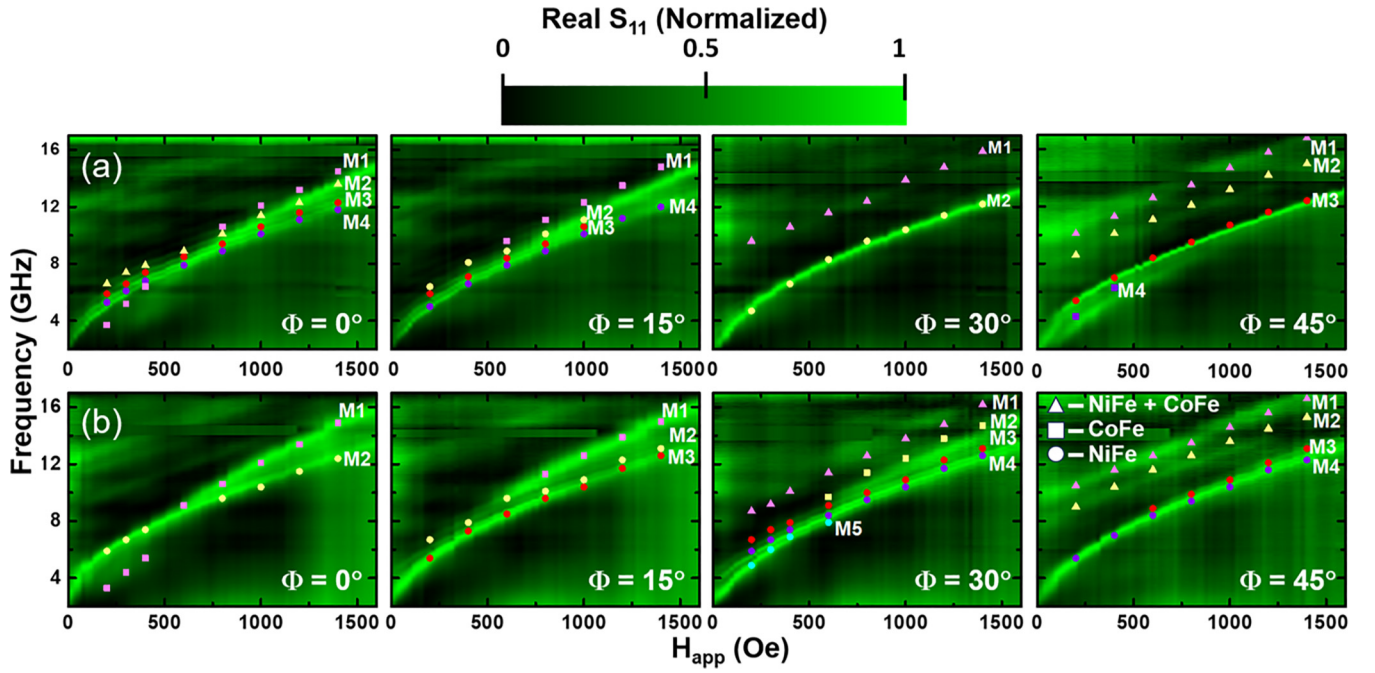


FIG. 2. Bias field (H_{app}) dependent SW absorption spectra of (a) square- and (b) circular-shaped BMC at different Φ values along with simulated results (symbols). The color map is shown at the top. The shape of the simulated points illustrates the spatial origin of the SW.

the spectrum at each H_{app} was subtracted from a reference spectrum (the spectrum at the highest value of H_{app}), resulting in a background-free signal [as illustrated in Fig. 1(d)]. The spectra collected from $H_{\text{app}} = 1600$ Oe to $H_{\text{app}} = 0$ Oe in 20-Oe intervals were collectively plotted in the form of a surface plot to obtain Fig. 2.

C. Micromagnetic simulations

To elucidate the experimental results, the micromagnetic simulations were performed using OOMMF software considering the 4×4 Py elements (circular and square shaped) mimicked from the scanning electron microscopy image, having the discrete cell size of $4 \times 4 \times 20$ nm³. The values of exchange stiffness constant (A) used were $A_{\text{CoFe}} = 3 \times 10^{-6}$ erg/cm, $A_{\text{Py}} = 1.3 \times 10^{-6}$ erg/cm, and $A_{\text{CoFe-Py}} = 2.1 \times 10^{-6}$ erg/cm for the interface between the Py-CoFe region. The saturation magnetization (M_s) values were set as $M_{s\text{CoFe}} = 1600$ emu/cc and $M_{s\text{Py}} = 800$ emu/cc. During the dynamic simulation, damping constant (α) values $\alpha_{\text{CoFe}} = 0.01$ and $\alpha_{\text{Py}} = 0.008$ were used. For both, the materials value of gyromagnetic ratio $\gamma = 18.5$ MHz/Oe and magneto-crystalline anisotropy $K = 0$ were taken. During simulation, the magnetization of the sample was saturated in one direction by applying a very high magnetic field and then the field was brought down to H_{app} after which the sample was relaxed to reach an equilibrium state. A square pulse in the transverse direction of H_{app} was applied which exerted the necessary torque to start the precessional magnetization dynamics.

III. RESULTS AND DISCUSSION

The experimental magnetic field dispersions of both square- and circular-shaped BMCs are shown in Fig. 2. It

is noteworthy that the manipulation of magnetic microstates, illustrated in Fig. 3, through precise adjustments in Φ or alterations in the Py inclusion shape, causes a substantial influence on the dynamic characteristics of the SWs.

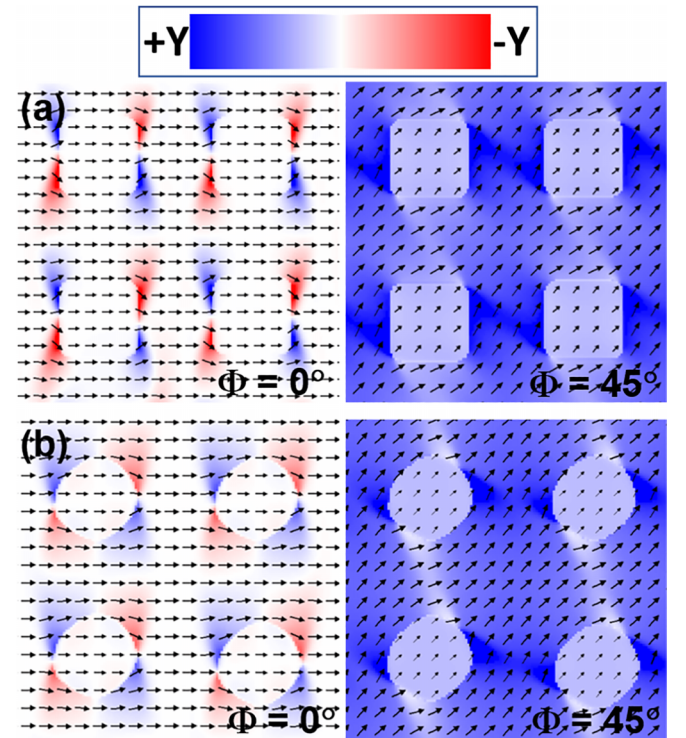


FIG. 3. The magnetic microstate for (a) square- and (b) circular-shaped BMC at $\Phi = 0^\circ$ and $\Phi = 45^\circ$ for $H_{\text{app}} = 200$ Oe, with the color map shown at the top of the images.

Furthermore, Figs. 3(a) and 3(b) illustrate the transition of the magnetic microstate as it depends on the shape and bias field angle, while maintaining a constant bias field magnitude ($H_{\text{app}} = 200$ Oe). These figures depict the evolution of the ground-state spins, initially trapped at the peripheries of square or circular dots, gradually aligning themselves with the effective bias field directions. This transformation of magnetic microstates, facilitated by adjustments of the bias field angle, induces a significant modulation in the demagnetizing fields. As a consequence, it gives rise to various uniform as well as nonuniform characteristics of magnetic field dispersion depicted in Fig. 2. The observed nonuniformity in the field dispersion of SW modes can be attributed to the coexistence of two distinct magnetic materials, Py and CoFe, each with their unique magnetic properties [36,50]. This nonuniform magnetic field dispersion of SW modes validates the theoretically predicted phenomenon of mode reversal [50], and this mode reversal is observed at $\Phi = 0^\circ$ for both square and circular BMCs. At $\Phi = 0^\circ$, the highest frequency mode, denoted as M1 (for $H_{\text{app}} > 600$ Oe), exhibits a nonmonotonic decrease in frequency with decreasing H_{app} . This reduction leads M1 to cross all lower frequency modes, eventually becoming the lowest frequency mode at lower H_{app} (below 600 Oe), thus causing mode reversal. The occurrence of mode reversal is highly dependent on the magnetic configuration and is observed exclusively at $\Phi = 0^\circ$. This phenomenon transforms into mode merging at $\Phi = 15^\circ$, regardless of the BMC's shape, as depicted in Figs. 2(a) and 2(b). A distinct variation in the number of SW modes and their characteristics is discerned as a result of the alteration in magnetic microstate brought about by changes in Φ , ranging from 0° to 45° . Interestingly, the nonuniformity in magnetic field dispersion completely vanishes at $\Phi = 30^\circ$ for the square-shaped BMC, accompanied with a reduction in the number of SW modes from four to two. In contrast, the circular-shaped BMC maintains its nonuniform dispersion characteristics, mainly due to the merging of the M2 mode with M3 at $\Phi = 30^\circ$. Moreover, it is worth noting that, at a fixed Φ , modifying the magnetic configuration by changing the Py inclusion's shape, as outlined in Fig. 3, results in the simultaneous retention and suppression of nonuniform field dispersion characteristics of SW modes. At $\Phi = 45^\circ$, the nonuniformity in field dispersion reappears, as evidenced by the splitting of mode M3 into M4 for the square-shaped BMC. In contrast, the circular-shaped BMC at $\Phi = 45^\circ$ exhibits nearly uniform field dispersion.

Some of the SW modes appear with low intensity in the SW absorption spectra due to challenges in VNA FMR measurements, especially with an increase in Φ . The increment in Φ leads to a reduction in the perturbing torque supplied by the radio frequency field, thereby impacting the signal-to-noise ratio and posing challenges in obtaining clear and intense modes at higher Φ ($\Phi = 30^\circ$ and $\Phi = 45^\circ$). However, despite their faint nature, these modes exhibit consistent frequency variations with the H_{app} and are well reproduced in the micromagnetic simulations, as shown in Fig. 2. For further clarification, the simulated surface plots of magnetic field dispersion have been shown in Fig. S1 of the Supplemental Material [51] which qualitatively reproduces all the major features observed in the experiment. However, the explicit values of the SW mode frequencies are not always

replicated due to limitations in the size of the simulated sample. Furthermore, incorporating exact edge roughness in the simulation is not always feasible, as discussed in the literature [37,38]. To elucidate the intrinsic characteristics of resonant SW modes, the spatial profiles of the dynamic magnetization components associated with these modes were examined. These profiles were scrutinized using the home-built MATLAB code DOTMAG [52], and a deeper understanding of the nature and behavior of the resonant SW modes was achieved. The frequency dependent preferential spatial confinement of SWs is readily observed at $H_{\text{app}} = 1000$ Oe. Lower frequency modes are primarily confined within Py regions, while the power in CoFe regions gradually increases with the increase in frequency, regardless of bias field angle and shape, as depicted in Figs. 4 and 5. The Py region, with a lower saturation magnetization (M_s) than CoFe, supports the excitation of lower frequency SW modes ($M_{\text{sPy}} = 800$ emu/cc and $M_{\text{sCoFe}} = 1600$ emu/cc). The spatial power profiles of SW modes exhibit interesting features that vary with H_{app} , depending on the region of excitation. The lower frequency SW modes, which exhibit maximum excitation in Py at higher H_{app} (> 600 Oe), show a gradual increase in power in the CoFe region as H_{app} is reduced. In contrast, the higher frequency SW modes, which have significant excitation in CoFe, display a highly anisotropic nature.

In the case of the square-shaped BMC at $\Phi = 0^\circ$, the power of the SW mode M1 remains predominantly concentrated in the CoFe channel across the entire range of H_{app} ($200 \text{ Oe} \leq H_{\text{app}} \leq 1000 \text{ Oe}$), experiencing a significant decrease in power within the Py region as H_{app} is reduced (as shown in Fig. 4). In contrast, the power of M2 increases within the Py region and shows a slight decrease within the CoFe channel as H_{app} decreases. The mode crossing of M1 with other modes, such as M2 and M3, indicates a mode reversal phenomenon, as the maximum power shifts to the CoFe region. At $\Phi = 15^\circ$, mode M1 primarily excites within the CoFe channel, although its power diminishes within the CoFe channel as H_{app} decreases. Notably, the spatial power profile at $\Phi = 30^\circ$, as depicted in Fig. 4, exhibits distinct characteristics compared to those observed at $\Phi = 0^\circ$ and $\Phi = 15^\circ$. The power distribution in both the Py and CoFe regions for the highest frequency mode, M1, is more uniform. At $\Phi = 45^\circ$, the powers of the high-frequency modes M1 and M2 are distributed all over the sample, consistent with the variation of H_{app} . The lowest frequency mode, M4, which appears for $H_{\text{app}} < 600$ Oe, displays maximum power within the CoFe channel perpendicular to H_{app} .

The investigation of spatial power profiles in circular- and square-shaped magnetically coupled BMCs reveals intriguing characteristics of the SW modes. In the circular BMC, the power distribution of the lower frequency mode predominantly concentrates in the Py region at high applied bias field ($H_{\text{app}} = 1000$ Oe), while gradually extending to the CoFe region as H_{app} decreases. Similarly, the highest frequency mode exhibits a power distribution pattern analogous to that observed in the square-shaped BMC. A notable finding emerges at $\Phi = 30^\circ$, where the spatial power profile of the M2 mode in the circular BMC displays a distinct behavior not observed in the square-shaped BMC at the same Φ . The power of the M2 mode primarily concentrates in the

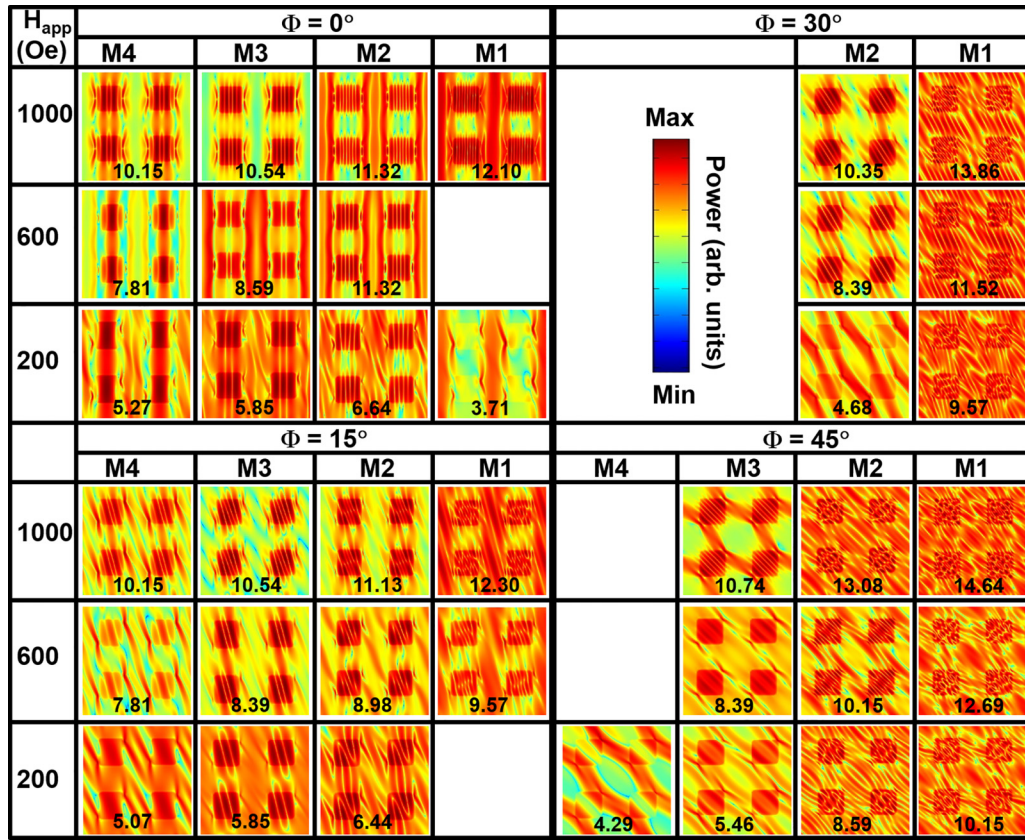


FIG. 4. The simulated power profile of different SW modes of the square-shaped BMC at different values of Φ and H_{app} , with the labeled mode frequency in gigahertz at the bottom of each profile.

Py-filled CoFe channel, extending beyond the next-to-next nearest neighbor in a direction perpendicular to H_{app} . This behavior is particularly prominent at high H_{app} (1000 Oe) but demonstrates a significant decrease in power within the CoFe region as H_{app} is reduced. The analysis also includes phase profiles and mode quantization details, as showcased in Supplemental Material [52] Figs S2 and S3, respectively, which highlights the presence of bias field dependent quantized, mixed quantized, and extended SW modes in both circular- and square-shaped BMCs. Overall, these findings contribute to a comprehensive understanding of the spatial power profiles of SW modes in different BMC configurations, emphasizing the influence of applied bias fields and mode quantization characteristics.

By examining the spatial excitation of SWs via power profiles presented in Figs. 4 and 5, we utilize the configuration of the simulated data points to convey the spatial source of the SWs, as illustrated in Fig. 2. This reveals that modes with maximum spatial confinement in CoFe exhibit a nonmonotonic decrease in frequency with H_{app} , leading to the nonuniform field dispersion of SWs. It is noteworthy to mention here that the spatial excitation of SWs in various regions of BMC is highly adjustable through the magnetic configuration. To understand the variation in spatial confinement of various SW modes with the variation of Φ and H_{app} , the demagnetizing field H_{de} and total energy density (E_d) distribution have been studied employing OOMMF micromagnetic simulation. The spatial maps of H_{de} at $H_{app} = 200$ Oe for the square BMC at $\Phi = 0^\circ, 15^\circ, 30^\circ$, and 45° are shown

in Fig. 6(a). At $\Phi = 0^\circ$, H_{de} is positive along the Py-CoFe channel, enhancing the overall field at that region, while it is negative along the CoFe channel, suppressing the overall field at that channel. On changing the orientation of H_{app} to $\Phi = 15^\circ$, the positive demagnetized channel retains its character, whereas the negative demagnetized channel gets fragmented to shorter channels aligned perpendicularly to the field direction. The fragmentation of negatively demagnetized channels leads to the breaking of long-range order, slightly reducing the impact of H_{de} along that channel. The absence of mode reversal at $\Phi = 15^\circ$ can be attributed to the distortion of the negatively demagnetized channel as the excitation of SWs now takes place in partially extended channels. At $\Phi = 30^\circ$, a new positively demagnetized channel passing through the Py nanodots perpendicular to H_{app} is created, along with the one present previously for $\Phi = 0^\circ$ and $\Phi = 15^\circ$. In this configuration, the negatively demagnetized region becomes confined between two positively demagnetized channels. The distortion of the positively demagnetized channels and the confinement of the negatively demagnetized channels play a crucial role in the significant reduction in the number of observed SW modes. This phenomenon is a direct result of the interplay between the geometry of the system and the distribution of demagnetization effects. The creation of completely new positively demagnetized channels connecting the diagonal Py nanodots (perpendicular to H_{app}) and negatively demagnetized channels parallel to those in the CoFe regions for $\Phi = 45^\circ$ is shown in Fig. 6(a). The creation of demagnetized channels again increases the number of modes, especially the lowest

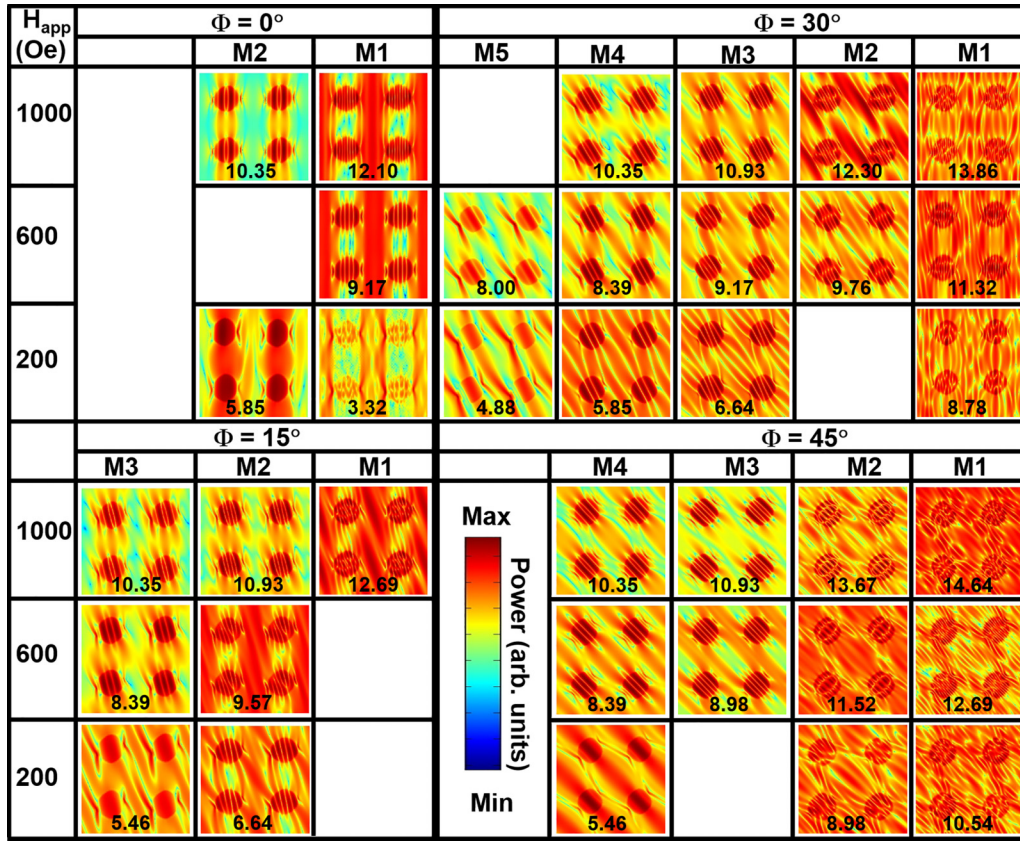


FIG. 5. The simulated power profile of various SW modes in the circular-shaped BMC at different values of Φ and H_{app} , with the labeled mode frequency in gigahertz at the bottom of each profile.

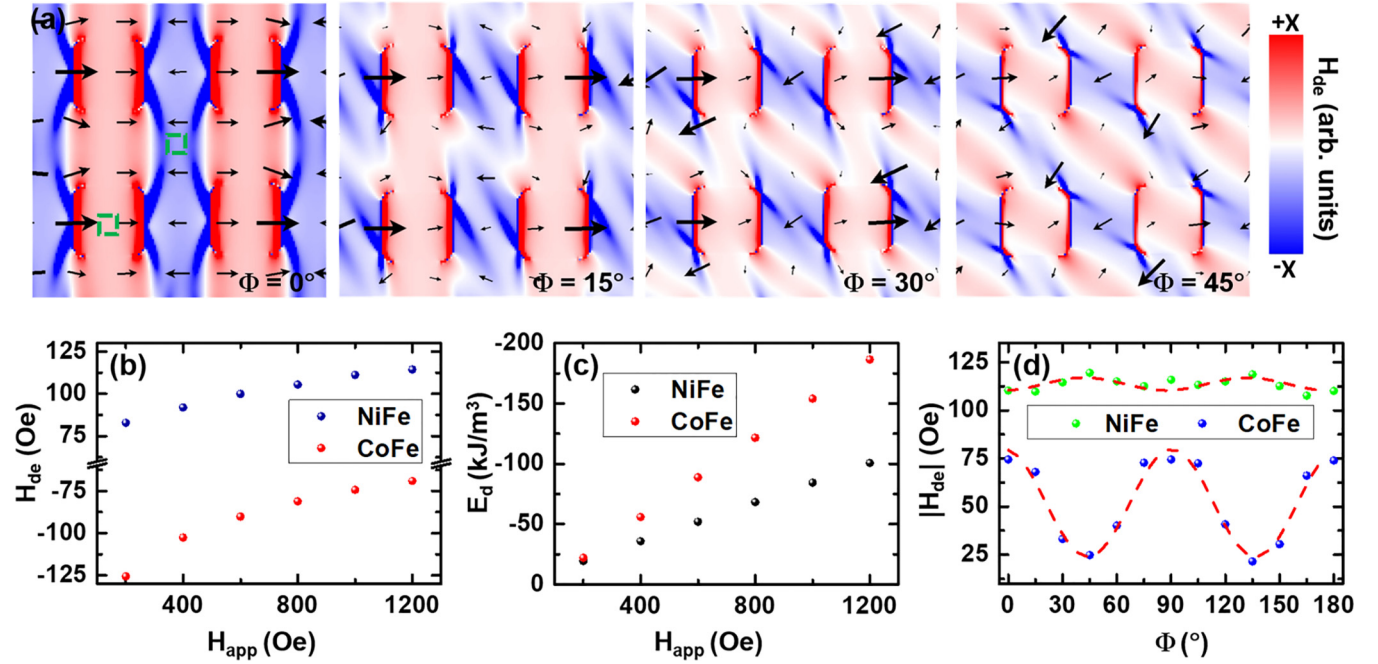


FIG. 6. (a) Spatial distribution of H_{de} at $H_{app} = 200$ Oe with the color map on the right. Variation of (b) H_{de} with H_{app} , (c) E_d with H_{app} at two regions shown by the dotted squares in (a), and (d) magnitude of H_{de} with Φ .

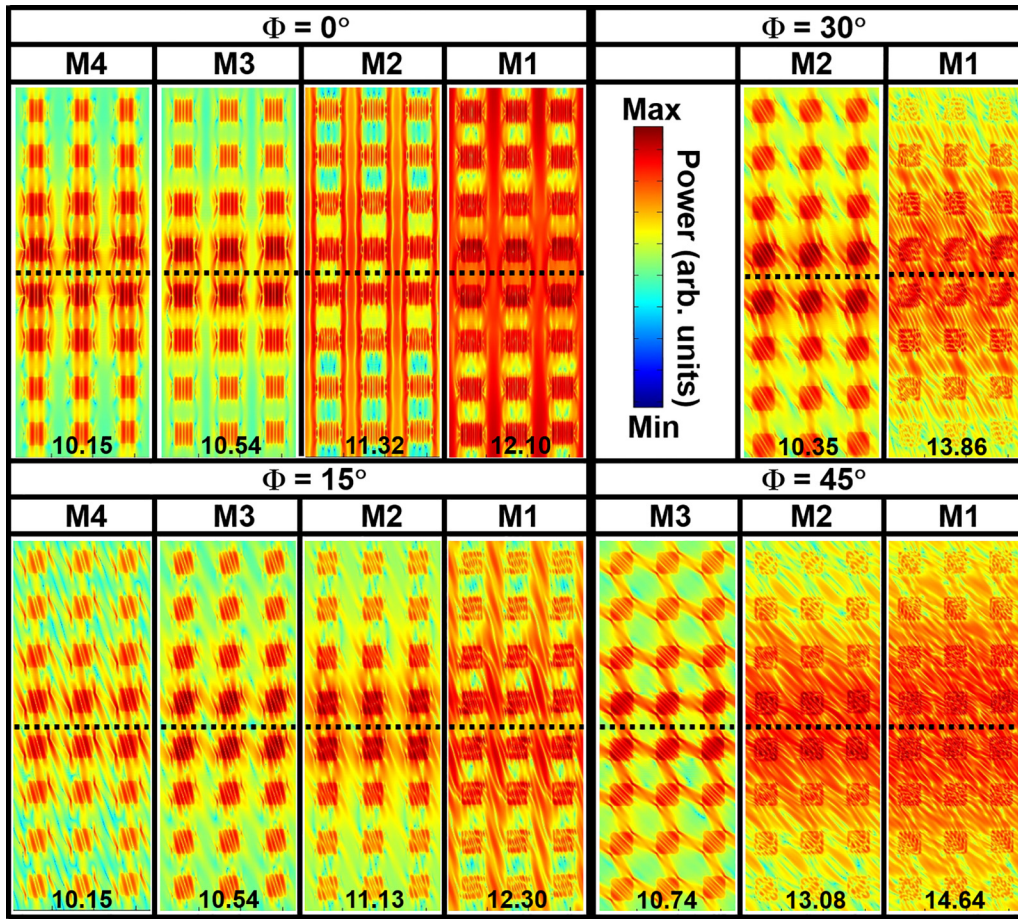


FIG. 7. The simulated power profile of the locally excited SW modes in square BMC at $H_{\text{app}} = 1000$ Oe for different Φ values, with the labeled mode frequency in gigahertz at the bottom of each profile. The line of excitation has been shown by a dotted line.

frequency mode M4, which appears at lower H_{app} and is mainly excited in the newly created negatively demagnetized channels.

At $\Phi = 0^\circ$ the variations of H_{de} with H_{app} at two regions [shown by green dotted squares in Fig. 6(a)] belonging to the positively demagnetized Py and negatively demagnetized CoFe regions are shown in Fig. 6(b). The magnitude of negative H_{de} increases sharply in the CoFe region with the reduction of H_{app} , whereas the magnitude of positive H_{de} decreases slowly with the reduction of H_{app} . The impact of the variation in H_{de} with H_{app} is clearly noticeable in the magnetic microstate, as depicted in Figs. S6 and S7 of the Supplemental Material [51]. The increasing impact of H_{de} with the reduction of H_{app} on the total energy density (E_{d}) is clearly evident in Fig. 6(c). CoFe, having a higher saturation magnetization, exhibits higher energy density at higher H_{app} . However, the energy density gap between Py and CoFe continuously decreases with the reduction of H_{app} and almost vanishes at 200 Oe. The gradual increment of power of lower frequency modes in the CoFe region with the reduction of H_{app} can be attributed to the increasing influence of negative H_{de} at lower H_{app} . At $H_{\text{app}} = 1000$ Oe, the variation of the magnitude of H_{de} with Φ in Py and CoFe is shown in Fig. 6(d) at two same regions [shown by green dotted squares in Fig. 6(a)]. H_{de} varies periodically in both regions with fourfold symmetry.

The line scans of H_{de} for each Φ at $H_{\text{app}} = 200$ Oe are shown in Fig. S4 of the Supplemental Material [51].

The change in shape from square to circular in the Py-filled region significantly affects H_{de} at the interface, leading to a variation in the number of modes at different Φ . The influence of the Py region's shape on H_{de} , resulting in the changes in the internal field, has been extensively discussed in a previous study [38]. The spatial distribution of the demagnetized channels in the circular BMC is similar to that observed in the square BMC configuration. The variation of H_{de} with H_{app} and Φ also follows a similar trend to that observed in the square BMC. For a more detailed analysis of H_{de} in the circular-shaped BMC, please refer to Fig. S5 in the Supplemental Material [51].

The SW propagation characteristics in the BMCs have been numerically studied using the OOMMF micromagnetic simulation by constructing a waveguide consisting of 4×8 square Py elements. Microwave excitation is applied at the center of the waveguide, indicated by a dotted line, utilizing a “sinc” function with a cut-off frequency of 30 GHz. Figure 7 displays the spatial power profiles of all the modes at various Φ values. Notably, the lower frequency SW mode, which exhibits maximum excitation in the Py region, propagates uniformly across the waveguide with minimal power loss regardless of Φ .

The higher frequency SW modes being significantly excited at the CoFe region, exhibit highly anisotropic propagation characteristics. At $\Phi = 0^\circ$, all the SW modes travel nearly uniformly to both ends of the waveguide without a loss of power (shown in Fig. 7). At $\Phi = 15^\circ$, higher frequency mode M1 shows a slight decrease in power towards the ends, whereas the lower frequency mode travels smoothly. For $\Phi = 30^\circ$, the SW intensity decays very fast and almost vanishes near the ends of the waveguide for high-frequency mode M1. At $\Phi = 45^\circ$, the intensity of high-frequency modes M1 and M2 decreases drastically near the ends of the waveguide. It is noteworthy to mention here that SWs exhibiting uniform excitation in both NiFe and CoFe regions rapidly decay in intensity, whereas those with maximum intensity in either NiFe or CoFe extend smoothly with minimal power loss. This exciting feature of SW propagation has a potential application as selective angular filters for high-frequency mode M1. Similar SW propagation properties have been observed for circular-shaped BMCs, which are shown in Fig. S8 of the Supplemental Material [51].

IV. CONCLUSIONS

In conclusion, our study sheds light on the crucial role of magnetic configuration in shaping the behavior of SWs in BMCs, specifically through ferromagnetic resonance experiments and micromagnetic simulations. We observed and reproduced the reversal of SW modes, wherein the mode with the highest frequency under higher applied bias fields shifts to

the lowest frequency as the bias field decreases. This reversal is highly dependent on the magnetic configuration, driven by magnetic microstates, transforming into mode merging and eventually disappearing as the in-plane bias field angle (Φ) changes from $\Phi = 0^\circ$ to $\Phi = 45^\circ$. The magnetic configuration significantly affects the SW characteristics, particularly in achieving mostly uniform field dispersion at $\Phi = 30^\circ$ for square BMCs and $\Phi = 45^\circ$ for circular BMCs, suppressing the nonuniform behavior caused by the contrasting magnetic properties of the constituents of the BMCs. The distribution of the demagnetizing field, coupled with variations in the applied bias field, plays a pivotal role in magnetic configuration dependent field dispersion and SW propagation characteristics. This comprehensive understanding of the interplay between configurational anisotropy and SW dynamics in BMCs holds promise for future magnonic device advancements.

ACKNOWLEDGMENTS

The authors acknowledge financial assistance from the Department of Science and Technology, Government of India under Grant No. DST/NM/TUE/QM-3/2019-1C-SNB and S.N. Bose National Centre for Basic Sciences, India under Grant No. SNB/AB/11-12/96. C.K. acknowledges S.N. Bose National Centre for Basic Sciences and P.K.P. acknowledges Council of Scientific & Industrial Research for support from their respective fellowships. The authors also acknowledge YoshiChika Otani and Ruma Mandal for assistance in fabricating the samples, and Arundhati Adhikari for assistance during the FMR measurement.

-
- [1] A. Barman *et al.*, The 2021 magnonics roadmap, *J. Phys.: Condens. Matter* **33**, 413001 (2021).
 - [2] A. Barman, S. Mondal, S. Sahoo, and A. De, Magnetization dynamics of nanoscale magnetic materials: A perspective, *J. Appl. Phys.* **128**, 170901 (2020).
 - [3] B. K. Mahato, S. Choudhury, R. Mandal, S. Barman, Y. Otani, and A. Barman, Tunable configurational anisotropy in collective magnetization dynamics of $\text{Ni}_{80}\text{Fe}_{20}$ nanodot arrays with varying dot shapes, *J. Appl. Phys.* **117**, 213909 (2015).
 - [4] D. Kumar, P. Sabareesan, W. Wang, H. Fangohr, and A. Barman, Effect of hole shape on spin-wave band structure in one-dimensional magnonic antidot waveguide, *J. Appl. Phys.* **114**, 023910 (2013).
 - [5] S. Mallick *et al.*, Tunability of domain structure and magnonic spectra in antidot arrays of Heusler alloy, *Phys. Rev. Appl.* **12**, 014043 (2019).
 - [6] Y. Cao, G. Yun, X. Liang, and N. Bai, Band structures of two-dimensional magnonic crystals with different shapes and arrangements of scatterers, *J. Phys. D: Appl. Phys.* **43**, 305005 (2010).
 - [7] S. Saha, R. Mandal, S. Barman, D. Kumar, B. Rana, Y. Fukuma, S. Sugimoto, Y. Otani, and A. Barman, Tunable magnonic spectra in two-dimensional magnonic crystals with variable lattice symmetry, *Adv. Funct. Mater.* **23**, 2378 (2013).
 - [8] A. De, K. Dutta, S. Mondal, S. Barman, Y. Otani, and A. Barman, Magnonic crystals with complex geometry, *Phys. Rev. B* **103**, 064402 (2021).
 - [9] S. Saha, S. Barman, S. Sugimoto, Y. Otani, and A. Barman, Tunable picosecond spin dynamics in two dimensional ferromagnetic nanodot arrays with varying lattice symmetry, *RSC Adv.* **5**, 34027 (2015).
 - [10] S. Choudhury, S. Barman, Y. Otani, and A. Barman, Efficient modulation of spin waves in two-dimensional octagonal magnonic crystal, *ACS Nano* **11**, 8814 (2017).
 - [11] H. Ulrichs, B. Lenk, and M. Münzenberg, Magnonic spin-wave modes in CoFeB antidot lattices, *Appl. Phys. Lett.* **97**, 092506 (2010).
 - [12] S. Majumder, S. Choudhury, S. Barman, Y. Otani, and A. Barman, Reconfigurable spin-wave dynamics in two-dimensional quasiperiodic magnonic crystals, *Physica E (Amsterdam, Neth.)* **134**, 114901 (2021).
 - [13] A. Kumar Mondal, S. Majumder, B. Kumar Mahato, S. Barman, Y. Otani, and A. Barman, Bias field orientation driven reconfigurable magnonics and magnon–magnon coupling in triangular shaped $\text{Ni}_{80}\text{Fe}_{20}$ nanodot arrays, *Nanotechnology* **34**, 135701 (2023).
 - [14] K. Dutta, A. De, S. Mondal, S. Barman, Y. Otani, and A. Barman, Dynamic configurational anisotropy in $\text{Ni}_{80}\text{Fe}_{20}$ antidot lattice with complex geometry, *J. Alloys Compd.* **884**, 161105 (2021).
 - [15] B. K. Mahato, B. Rana, R. Mandal, D. Kumar, S. Barman, Y. Fukuma, Y. Otani, and A. Barman, Configurational anisotropic spin waves in cross-shaped $\text{Ni}_{80}\text{Fe}_{20}$ nanoelements, *Appl. Phys. Lett.* **102**, 192402 (2013).

- [16] P. K. Pal, S. Majumder, Y. Otani, and A. Barman, Bias-field tunable magnon-magnon coupling in $\text{Ni}_{80}\text{Fe}_{20}$ nanocross array, *Adv. Quantum Technol.* **6**, 2300003 (2023).
- [17] S. Pal, P. K. Pal, R. Fahiha, S. Bandyopadhyay, and A. Barman, Acousto-plasmo-magnonics: Coupling spin waves with hybridized phonon-plasmon waves in a 2D artificial magnonic crystal deposited on a plasmonic material, *Adv. Funct. Mater.* **33**, 2304127 (2023).
- [18] D. A. Bozhko, V. I. Vasyuchka, A. V. Chumak, and A. A. Serga, Magnon-phonon interactions in magnon spintronics (Review article), *Low Temp. Phys.* **46**, 383 (2020).
- [19] T. Schwarze and D. Grundler, Magnonic crystal wave guide with large spin-wave propagation velocity in CoFeB , *Appl. Phys. Lett.* **102**, 222412 (2013).
- [20] P. A. Popov, A. Y. Sharaevskaya, E. N. Beginin, A. V. Sadovnikov, A. I. Stognij, D. V. Kalyabin, and S. A. Nikitov, Spin wave propagation in three-dimensional magnonic crystals and coupled structures, *J. Magn. Magn. Mater.* **476**, 423 (2019).
- [21] S.-K. Kim, K.-S. Lee, and D.-S. Han, A gigahertz-range spin-wave filter composed of width-modulated nanostrip magnonic-crystal waveguides, *Appl. Phys. Lett.* **95**, 082507 (2009).
- [22] A. V. Sadovnikov, V. A. Gubanov, S. E. Sheshukova, Y. P. Sharaevskii, and S. A. Nikitov, Spin-wave drop filter based on asymmetric side-coupled magnonic crystals, *Phys. Rev. Appl.* **9**, 051002(R) (2018).
- [23] R. Silvani, M. Kostylev, A. O. Adeyeye, and G. Gubbiotti, Spin wave filtering and guiding in Permalloy/iron nanowires, *J. Magn. Magn. Mater.* **450**, 51 (2018).
- [24] S. A. Odintsov, S. E. Sheshukova, S. A. Nikitov, E. H. Lock, E. N. Beginin, and A. V. Sadovnikov, Nonreciprocal spin wave propagation in bilayer magnonic waveguide, *J. Magn. Magn. Mater.* **546**, 168736 (2022).
- [25] A. A. Martyshev, E. N. Beginin, A. I. Stognij, S. A. Nikitov, and A. V. Sadovnikov, Vertical spin-wave transport in magnonic waveguides with broken translation symmetry, *IEEE Magn. Lett.* **10**, 1 (2019).
- [26] A. V. Sadovnikov, A. A. Zyablovsky, A. V. Dorofeenko, and S. A. Nikitov, Exceptional-point phase transition in coupled magnonic waveguides, *Phys. Rev. Appl.* **18**, 024073 (2022).
- [27] Y. Zhu, K. H. Chi, and C. S. Tsai, Magnonic crystals-based tunable microwave phase shifters, *Appl. Phys. Lett.* **105**, 022411 (2014).
- [28] S. Mayr *et al.*, Spin-wave emission from vortex cores under static magnetic bias fields, *Nano Lett.* **21**, 1584 (2021).
- [29] S. Wintz, V. Tiberkevich, M. Weigand, J. Raabe, J. Lindner, A. Erbe, A. Slavin, and J. Fassbender, Magnetic vortex cores as tunable spin-wave emitters, *Nat. Nanotechnol.* **11**, 948 (2016).
- [30] T. Brächer, O. Boulle, G. Gaudin, and P. Pirro, Creation of unidirectional spin-wave emitters by utilizing interfacial Dzyaloshinskii-Moriya interaction, *Phys. Rev. B* **95**, 064429 (2017).
- [31] A. Adhikari, C. Banerjee, A. Kumar Mondal, A. K. Chaurasiya, S. Choudhury, J. Sinha, S. Barman, and A. Barman, Anisotropic spin-wave propagation in asymmetric width modulated $\text{Ni}_{80}\text{Fe}_{20}$ nanostripes, *Mater. Sci. Eng., B* **272**, 115385 (2021).
- [32] A. A. Nikitin, A. B. Ustinov, A. A. Semenov, A. V. Chumak, A. A. Serga, V. I. Vasyuchka, E. Lähderanta, B. A. Kalinikos, and B. Hillebrands, A spin-wave logic gate based on a width-modulated dynamic magnonic crystal, *Appl. Phys. Lett.* **106**, 102405 (2015).
- [33] A. V. Chumak, A. A. Serga, and B. Hillebrands, Magnon transistor for all-magnon data processing, *Nat. Commun.* **5**, 4700 (2014).
- [34] D. Kumar, S. Barman, and A. Barman, Magnetic vortex based transistor operations, *Sci. Rep.* **4**, 4108 (2014).
- [35] A. Khitun, M. Bao, and K. L. Wang, Magnetic cellular nonlinear network with spin wave bus for image processing, *Superlattices Microstruct.* **47**, 464 (2010).
- [36] A. Adhikari, S. Majumder, Y. Otani, and A. Barman, Active control of dipole-exchange coupled magnon modes in nanoscale bicomponent magnonic crystals, *ACS Appl. Nano Mater.* **6**, 7166 (2023).
- [37] S. Choudhury, S. Pan, S. Barman, Y. Otani, and A. Barman, Anisotropic spin waves in two-dimensional triangular shaped bi-component magnonic crystal, *J. Magn. Magn. Mater.* **490**, 165484 (2019).
- [38] S. Choudhury, S. Saha, R. Mandal, S. Barman, Y. Otani, and A. Barman, Shape- and interface-induced control of spin dynamics of two-dimensional bicomponent magnonic crystals, *ACS Appl. Mater. Interfaces* **8**, 18339 (2016).
- [39] G. Duerr, M. Madami, S. Neusser, S. Tacchi, G. Gubbiotti, G. Carlotti, and D. Grundler, Spatial control of spin-wave modes in $\text{Ni}_{80}\text{Fe}_{20}$ antidot lattices by embedded Co nanodisks, *Appl. Phys. Lett.* **99**, 202502 (2011).
- [40] Z. K. Wang, V. L. Zhang, H. S. Lim, S. C. Ng, M. H. Kuok, S. Jain, and A. O. Adeyeye, Nanostructured magnonic crystals with size-tunable bandgaps, *ACS Nano* **4**, 643 (2010).
- [41] J. W. Klos, M. L. Sokolovskyy, S. Mamica, and M. Krawczyk, The impact of the lattice symmetry and the inclusion shape on the spectrum of 2D magnonic crystals, *J. Appl. Phys.* **111**, 123910 (2012).
- [42] M. Krawczyk, S. Mamica, M. Mruczkiewicz, J. W. Klos, S. Tacchi, M. Madami, G. Gubbiotti, G. Duerr, and D. Grundler, Magnonic band structures in two-dimensional bi-component magnonic crystals with in-plane magnetization, *J. Phys. D: Appl. Phys.* **46**, 495003 (2013).
- [43] F. S. Ma, H. S. Lim, Z. K. Wang *et al.*, Micromagnetic study of spin wave propagation in bicomponent magnonic crystal waveguides, *Appl. Phys. Lett.* **98**, 153107 (2011).
- [44] S. Tacchi, G. Duerr, J. W. Klos, M. Madami, S. Neusser, G. Gubbiotti, G. Carlotti, M. Krawczyk, and D. Grundler, Forbidden band gaps in the spin-wave spectrum of a two-dimensional bicomponent magnonic crystal, *Phys. Rev. Lett.* **109**, 137202 (2012).
- [45] G. Gubbiotti, S. Tacchi, M. Madami, S. N. Piramanayagam, S. C. Ng, and M. H. Kuok, Collective spin waves in a bicomponent two-dimensional magnonic crystal, *Appl. Phys. Lett.* **100**, 162407 (2012).
- [46] C. S. Lin, H. S. Lim, Z. K. Wang, S. C. Ng, and M. H. Kuok, Band gap parameters of one-dimensional bicomponent nanostructured magnonic crystals, *Appl. Phys. Lett.* **98**, 022504 (2011).
- [47] M. Langer *et al.*, Role of internal demagnetizing field for the dynamics of a surface-modulated magnonic crystal, *Phys. Rev. B* **95**, 184405 (2017).
- [48] S. Mamica, M. Krawczyk, and D. Grundler, Nonuniform spin-wave softening in two-dimensional magnonic crystals as a tool

- for opening omnidirectional magnonic band gaps, *Phys. Rev. Appl.* **11**, 054011 (2019).
- [49] S. Mamica and M. Krawczyk, Reversible tuning of omnidirectional band gaps in two-dimensional magnonic crystals by magnetic field and in-plane squeezing, *Phys. Rev. B* **100**, 214410 (2019).
- [50] S. Mamica, Influence of the demagnetizing field on the spin-wave softening in bicomponent magnonic crystals, *J. Magn. Mater.* **546**, 168690 (2022).
- [51] See Supplemental Material at <http://link.aps.org/supplemental/10.1103/PhysRevB.109.075407> for (i) simulated magnetic field dispersion, (ii) spin-wave phase profile, (iii) simulated demagnetizing field analysis, (iv) magnetic microstate, and (v) spin-wave propagation.
- [52] D. Kumar, O. Dmytriiev, S. Ponraj, and A. Barman, Numerical calculation of spin wave dispersions in magnetic nanostructures, *J. Phys. D: Appl. Phys.* **45**, 015001 (2012).